Article

From Nanoscale to Macroscale Characterization of Sulfur-Modified Oxidized Carbon Nanotubes in Styrene Butadiene Rubber Compounds

Pilar Posadas,* Pilar Bernal-Ortega, M. Mar Bernal, Aurora Nogales, Rodrigo Navarro, and Juan L. Valentín
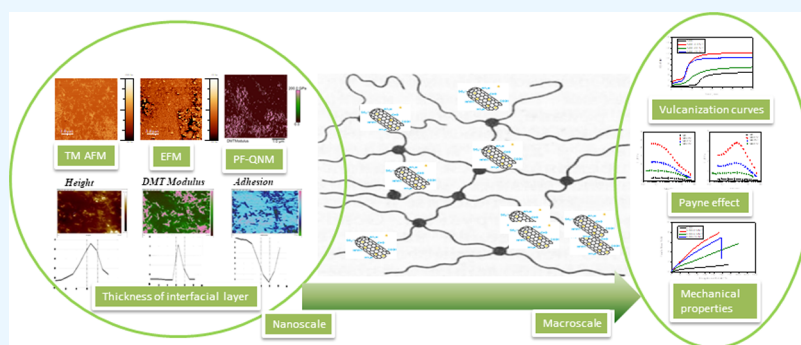
Read Online

ACCESS | Metrics & More | Article Recommendations

ABSTRACT: The homogeneous dispersion of carbon nanotubes (CNTs) in a rubber matrix is a key factor limiting their amazing potential. CNTs tend to agglomerate into bundles due to van der Waals interactions. To overcome this limitation, CNTs have been surface-modified with oxygen-bearing groups and sulfur. Using atomic force microscopy (AFM) techniques, a deep nanoscale characterization of the morphology, the degree of dispersion of the CNTs in the styrene butadiene rubber (SBR) matrix, and the thickness of the interfacial layer was carried out in this study. In this context, the results from nanoscale characterization showed that the thermal oxidation-sulfur treatment leads to a composite with better dispersion in the matrix, as well as a thicker interfacial layer, indicating a stronger filler−rubber interaction. The second part of this work focused on the macroscale results, such as the Payne effect, vulcanization curves, and mechanical properties. The Payne effect, vulcanization curves, and mechanical properties confirmed the lower reinforcing effect observed in the case of the chemical oxidation treatment because, on the one hand, this composite showed the highest agglomeration of CNTs after the acid treatment. On the other hand, the presence of acid residues provoked the absorption of basic accelerators on the surface of the CNTs.

1. INTRODUCTION

Elastomers are of great importance in industry due to their high elasticity and being capable of recovering their original state after being stretched. Styrene butadiene rubber (SBR) is the most globally produced synthetic rubber, and its main application is in the manufacturing of tires, but it also has other applications such as cover trips, wires, footwear, roofing barriers, and sport goods.[1−3] Traditionally, conventional fillers such as carbon black, silica, and clays are added into rubber matrices with the aim to improve the mechanical,[4−6] barrier,[7−9] and tear properties.[10] Both dispersion and orientation of a filler into the matrix, the size, and the aspect ratio of the particles as well as the interfacial interactions between the organic and inorganic phases have been shown to have a large influence on the mechanical behavior of the final compounds.[11] The main problem with conventional fillers is that the addition of high amounts of particles is needed to achieve the requirements of the final product.[12] This causes some disadvantages, such as the increase in the weight of the material, the poor interaction between the matrix and the filler, and the strong filler networking.[10]

The use of nanoparticles has been extended in the field of lightweight material field. Their high surface area combined with their low density allows obtaining excellent mechanical properties with low filler loadings and, therefore, a lower weight.[13] Nanofillers include spherical particles such as silica[14]

or titania,[15] platelets such as layered silicates,[16] carbon,[17] and multiwall or single-wall[10,11,13,18−23] carbon nanotubes (CNTs). CNTs exhibit unique electronic properties and high thermal conductivity, as well as excellent mechanical properties such as stiffness, strength, and resilience, which exceed those of any current material.[24] Their exceptional properties are due to the cylindrical arrangement of the graphite sheets, in conjunction with their large aspect ratio.[13] Despite the amazing potential of CNTs, achieving a homogeneous dispersion of these particles in a polymer matrix is one of the major challenges. The weak forces that hold CNTs together, such as van der Waals and $\pi-\pi$ interactions, cause the tubes to become entangled and form large agglomerates. For this reason, the expected improvement in the properties of the final compound is reduced.[13,25] In order to improve CNT disentanglement and dispersion in the elastomer matrix, several investigations have been carried out.[26−33] There are two main approaches commonly used based on mechanical dispersion methods and surface modification.[34−38] In this framework, one strategy to improve the dispersion of CNTs into elastomer matrices is the modification of the CNT surface by oxidation-sulfur treatment. This process introduces functional groups to the surface that are capable of interaction with the polymer chains. In this work, the modification treatment was carried out in two steps. First, nanoparticles are oxidized to introduce oxygen-bearing groups on the surface using two different methods. The oxidized CNTs were then modified with sulfur.[39] Both modified CNTs were incorporated into the SBR matrix and compared with the unmodified CNT-SBR composite with the same filler content. As previously explained above, the degree of dispersion of nanotubes within the polymer matrix is a key factor to substantiate their effect on the in-rubber properties. Therefore, the nanoscale characterization of the nanoparticle dispersion was performed using two different atomic force microscopy (AFM) techniques: tapping mode atomic force microscopy (TP-AFM)[1,13] and electronic force microscopy (EFM).[40]

The strong interfacial interaction between the nanotubes and the elastomer matrix is another important factor in the achievement of high-performance CNT elastomer nanocomposites.[41] The most commonly used method to evaluate the interfacial interaction between fillers and elastomers[42,43] is based on determining the content of bound rubber, which is defined as a polymer film of a few nanometers[44,45] fixed at the particle rubber interface and is therefore resistant to dissolution in a solvent. The higher content of bound rubber suggests a stronger interfacial interaction. Nevertheless, these measurements can only be done on unvulcanized compounds and, therefore, do not take into account the rubber−filler interactions that occur during vulcanization. In addition, other methods such as nuclear magnetic resonance spectroscopy (NMR),[46−48] dynamic mechanical analysis (DMA),[49,50] dielectric relaxation spectrum (DRS),[50−54] and Raman spectroscopy (RS)[55,56] have been used for the study of vulcanized compounds and their relationship with the final properties of the compound. In this sense, atomic force microscopy is also a significant tool to study the interphase.[45,57] For instance, some authors used the difference in the width detected in phase and height images to evaluate the thickness of bonded rubber.[45,58]

In recent years, a new AFM technique called peak force quantitative nanomechanical mapping (PF-QNM) has been used to measure the thickness of the interphase rubber−filler. This method allows mapping of the nanomechanical proper-ties, such as adhesive force, elastic modulus, and deformation, simultaneously with topography at the same special reso-lution.[59−62] In this study, three different SBR compounds filled with pristine and sulfur-functionalized CNTs were prepared. A systematic study of the dispersion of these particles, by AFM and EFM analyses, was carried out to obtain a better understanding of the final properties of SBR/CNT com-pounds. In addition, the interfacial layer thicknesses of the three different vulcanized materials were measured by AFM PF-QNM. Finally, the Payne effect, vulcanization process, and mechanical properties of the three composites were also examined to correlate results obtained at the nanoscale level with conventional macroscale-level techniques.

2. EXPERIMENTAL SECTION

2.1. Materials. The s-SBR used in this work was acquired from Lanxess (Buna 5025-0). According to the manufacturer, s-SBR has styrene and vinyl contents of 25 and 50%, respectively. A conventional sulfur vulcanization system was used, maintaining the accelerant/sulfur ratio (1:2) constant, with a constant sulfur content of 1 phr (1 part per hundred rubber −100 phr). The amount of free sulfur added to the modified CNTs was different depending on the amount of sulfur chemically bound to the CNT surface for each reaction performed, with the aim of keeping the sulfur content constant (1 phr: 1 part per hundred rubber-100 phr).[39] Additionally, N-cyclohexyl-2-benzothiazolesulfenamide (CBS) as an acceler-ator and zinc oxide (3 phr) and stearic acid (3 phr) rubber grade as activators were added. The nanofillers used were multiwall carbon nanotubes with the trade name *NC7000* from *Nanocyl S.A. (Belgium)* with the following properties: average diameter 9.5 mm, average length 1.5 μm, surface area 250−300 $m^2 \cdot g^{-1}$, and carbon purity 90%.

2.2. Oxidation and Functionalization with Elemental Sulfur of CNTs. *2.2.1. Chemical Oxidation.* Chemical oxidation consisted of treating CNTs with a 3:1 concentrated sulfuric/nitric acid mixture H_2SO_4 (95% purity)/HNO_3 (95% purity), both from Sigma-Aldrich (Madrid, Spain), refluxed at 70 °C for 2 h. The nanotubes were then filtered through a glass filter funnel with a PTFE membrane (0.2 μm pore size, Millipore, Burlington, MA) and washed several times with distilled water to neutral pH. Next, nanoparticles were dried at 80 °C for 24 h. The procedure was continued by adding 150 mL of hydrogen peroxide (H_2O_2) supplied by Sigma-Aldrich to the nanotubes. After that, the mixture was sonicated for 2 h and filtered at room temperature. Then, the chemically oxidized CNTs were dried again at 80 °C for 24 h. In accordance with the published literature,[63−66] chemical oxidation leads to the introduction of carboxyl (COOH), hydroxyl (OH), and carbonyl groups (C=O) when sulfuric acid and nitric acid are combined. In addition, the treatment with H_2O_2 may increase the density of C=O groups.[63]

2.2.2. Thermal Oxidation. Thermal oxidation of CNTs was performed in a quartz tube reactor inside of a furnace. Nanoparticles were introduced into a quartz tube at 300 °C for 45 min under an oxygen atmosphere. The oven was then cooled to room temperature, after which the oxidized CNTs were removed from the quartz tube and stored in a sealed container in the air.

2.2.3. Elemental Sulfur Functionalization. After oxidation, CNT functionalization was carried out by reacting elemental sulfur into the groups introduced in the oxidation process, according to the following procedure: first, using carbon

disulfide (CS2) as a solvent to form a dispersing solution, each oxidized CNT and sulfur were sonicated together for 2 h. The solvent was then evaporated under reduced pressure. The reaction was then adjusted to 155 °C using an oil bath and heated under a vacuum for 2 h to complete the reaction. Finally, the functionalized nanotubes were successively washed to remove any nongrafted sulfur species.

The modification of CNT was carried out with the aim of obtaining better rubber−filler interactions and also a more efficient use of the sulfur in the vulcanization process, as was explained in previous work.[39] The CNTs were designated as follows: UCNT for the unmodified CNT, CCNT for the CNT with chemical oxidation sulfur modification, and TCNT for the CNT with thermal oxidation-sulfur modification treatment; the filler loading was 10 phr in the three composites, and one compound without filler was prepared too.

2.3. Preparation of Nanocomposites. SBR compounds were prepared on a Gumix laboratory two-roll mill. The cylinder diameter and length were 15 and 30 cm, respectively, with a friction ratio of 1:1.15. The rolls were kept cold during the mixing process by means of a cold water circulation system. The samples were vulcanized in a hydraulic press at 160 °C for the optimum vulcanization time, t97, in accordance with the rheometer curves (RPA 2000). To obtain a flat surface for AFM and EFM analysis, the sheet sample was sectioned with a Leica EM UC6 ultramicrotome at −150 °C.

The compounds were labeled as follows: SBR-UCNT (for the unmodified CNT compound), SBR-CCNT (for the compound with chemical oxidation sulfur modification of CNT), and SBR-TCNT (for the compound with thermal oxidation sulfur modification of CNT).

2.4. Characterization of Nanocomposites. *2.4.1. Scanning Electron Microscopy (SEM) Analysis.* Ultrahigh field emission scanning electronic microscopy FESEM was employed to determine the morphology of the three different nanotubes, pristine and modified. To determine how the different treatments affected the structure of the particles, an analysis of the different SEM images using ImageJ software (W.S. Rasband, US. National Institute of Health, Bethesda) was performed.

2.4.2. Atomic Force Microscopy (AFM). Atomic force microscopy images were acquired on a Multimode AFM microscope (Veeco Instruments, Santa Barbara, CA) with a NanoScope IVa controller (software version 6.14r). The measurements were taken place under ambient conditions at room temperature with the purpose of characterizing the morphology at nanometric scale. A silicon tapping probe (RTEST, Vecco) was used for the measurements, possessing a spring constant of 42 N/m. The set point ratio was 0.7 because tip−sample forces were small, and it is not necessary to consider the effect of the contact area between them in light or moderate tapping.[1] Hence, brighter areas in the phase image correspond to CNTs. The cantilever was made of Si_3N_4 and oscillated at a resonance frequency of ∼300 kHz. Samples were scanned over square regions of 5 and 2 μm size. At least 3 different positions were scanned for each sample at a resolution of 512 × 512 pixels.

To obtain a very smooth surface of the bulk rubber compounds for the AFM analysis, the samples were first cooled to temperatures below their glass transition temperatures using liquid nitrogen and then sectioned by using a diamond blade attached to a cryo-ultramicrotome Leica UEM UC6/EM FC6.

From the height images in five different 5 μm × 5 μm images, the average roughness R_a (the arithmetic average of the absolute values of the surface height deviation measured from the mean plane) and R_q (the root-mean-square average of the surface height deviation taken from the mean data) were calculated. The images were analyzed by means of nanoscope image processing software.

2.4.3. Electric Force Microscopy (EFM). To minimize topography effects on the electrostatic force gradient signal, two scans were performed during EFM measurements. In the first scan, a topographic profile was obtained by intermittent contact of the tip with the sample surface. The tip was then lifted to a predetermined height. The lift height was chosen to ensure no topology influence in ambient conditions and was 150 nm. The second scan was performed at a constant distance, following the sample topographic profile, where the biased tip−sample interaction affected the oscillation phase of the vibrating cantilever. Electrostatic force gradient images were generated by detecting and processing changes in the phase shifts.[67] An integrated Co/Cr-coated magnetic force-etched silicon probe tip with a resonant frequency of around 75 kHz was used. Imaging was performed in tapping mode by measuring the electric field gradient distribution across the sample surface by applying a voltage to the cantilever tip. Tip bias voltages were varied from −7 to 7 V at a constant tip−sample distance of 150 nm. Different regions of the samples were scanned to obtain reproducible results for the materials studied. Images of SBR compounds were analyzed by using Nanoscope 6 software. All measurements were performed under ambient conditions at room temperature using a standard cantilever holder.

2.4.4. Atomic Force Microscopy Nanoindentation Measurements. To select the appropriate region for studying the interphase between the CNT and rubber, two force−distance curves were required: one for one isolated CNT and another for the matrix. An AFM force−distance curve is a plot that represents the force−distance relationship between the AFM tip and the sample surface, where the separation distance is controlled by a closed-loop scanning system of the AFM during the measurements.[68] The interacting force measured in air is usually the van der Waals force.[69] After a complete AFM tip engagement process, including an approach and separation cycle, the curves can be plotted.

Peak force quantitative nanomechanical mapping (PF-QNM) nanoindentation measurements of samples were evaluated by using a Bruker Multimode 8 with a Nanoscope V controller. In this mode, the probe makes brief contact with the surface of a sample and a force−distance curve is recorded at each pixel of the image, and the force−distance curve is used for generating an image.[41] At the beginning of this curve, the tip is far from the surface. There is no interaction between the tip and surface in this region. When the tip is close enough to the surface, an attractive force exists between them. Typically, the gradient of the attractive force is much greater than the spring constant of the cantilever. As a result, the tip is bent toward the surface to make a tip−surface contact. Once contact is made between the tip and the sample, an adhesion is established between them. The retraction cycle begins when the force used to pull the tip away from the surface exceeds the adhesive force between them. This pull-off force can be used as a measure of the adhesion.[41,70] By fitting a portion of the retrace force curve using an appropriate contact mechanics model such as Hertz, Johnson−Kendall−Roberts (JKR), or

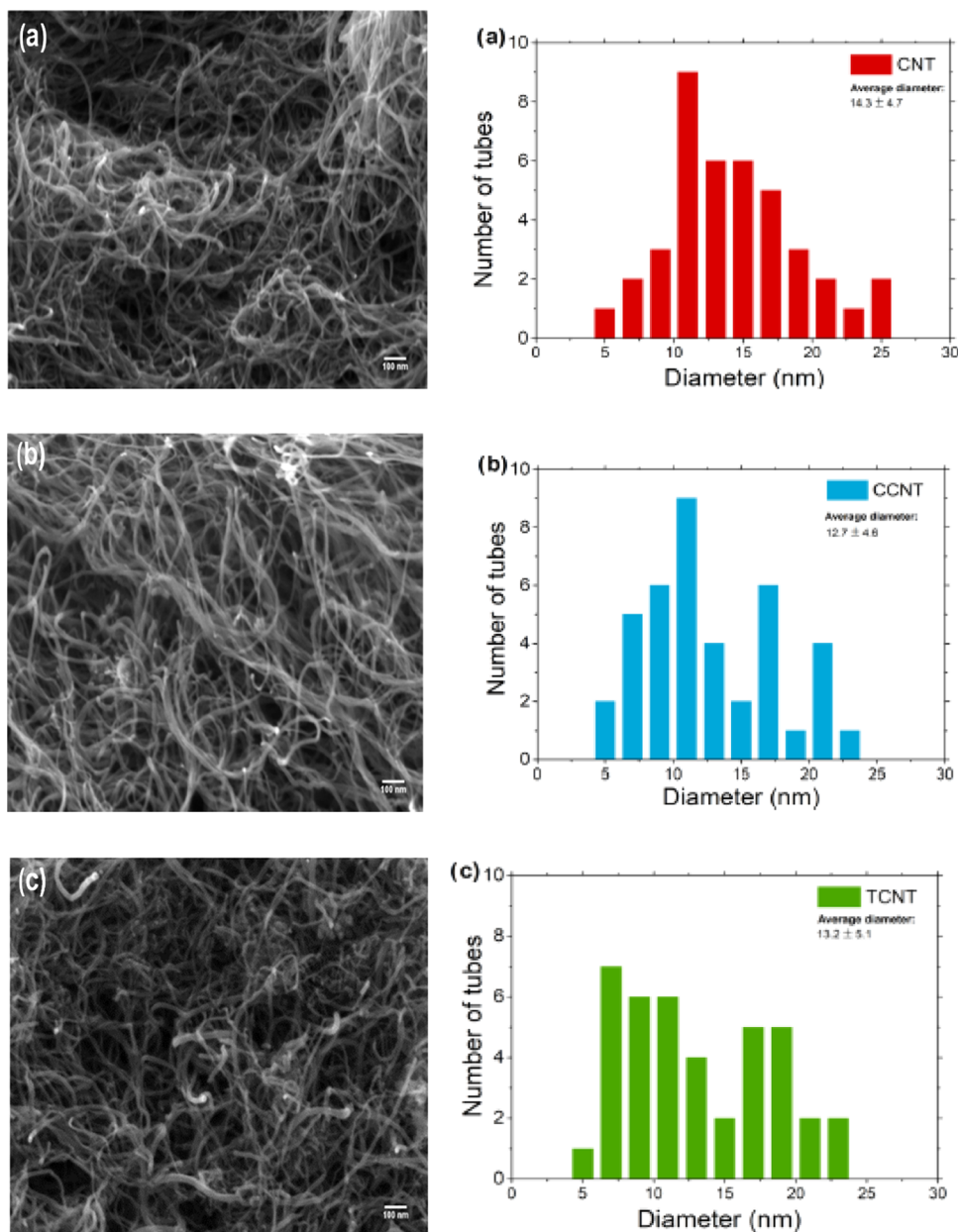**Figure 1.** FESEM images at a 100 μm resolution of (a) unmodified CNT and its diameter distribution, (b) CCNT and its diameter distribution, and (c) TCNT and its diameter distribution.

Deriaguin–Muller–Toporov (DMT), Young's modulus of the specimen surface is extracted.[71]

The samples were cut according to the same procedure described in Section 2.4.2. All quantitative measurements were performed at room temperature, by using a Scanasyst-air (Bruker) probe. The cantilever spring constant was measured using the thermal tune method and was found to be approximately 0.45–0.98 N/m. The tip radius was calibrated against a polystyrene standard by taking into account the DMT model[72] via eq 1

$$E_r = \frac{3(F_{tip} - F_{adh})}{4\sqrt{R_d^3}}$$

(1)

where E_r is the reduced Young modulus, F_{tip} is the force on the tip, F_{adh} is the adhesive force between the AFM tip and the sample, R is the AFM tip radius, and d is the penetration depth.

The reduced modulus and Young's modulus are related by eq 2, assuming that the tip Young's modulus is much higher than the sample Young's modulus

$$E_s = \frac{E_r}{1 - \nu_s^2}$$

(2)

where ν is the Poisson's ratio value.

The exact experimental procedure was as follows: based on the supplier's specification, an initial F_{tip} was set, and an initial estimate of the tip radius was taken into account. The F_{tip} was chosen to generate a deformation depth of approximately 5 nm since F_{adh} could be neglected under these experimental conditions. An experiment was then performed on the polystyrene standard. The value of the tip radius was systematically modified until the measured Young's modulus of the reference matched the one provided by the supplier. The value obtained for the tip radius was typically around 10 nm.
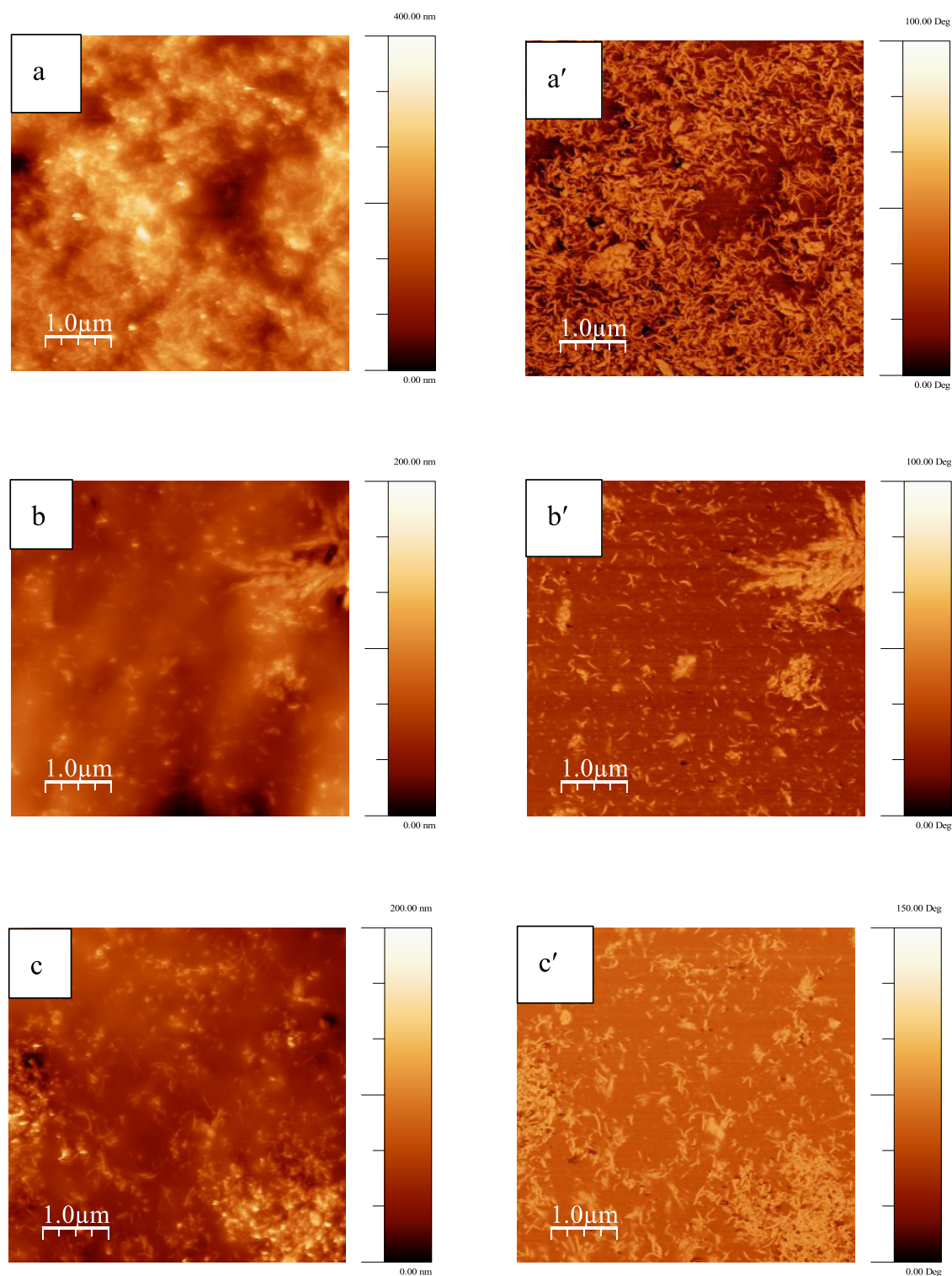
Figure 2. Tapping mode AFM 5 × 5 μm^2 images of SBR-UCNT (a) height image and (a') phase image, SBR-CCNT (b) height image and (b')
phase image, and SBR-TCNT (c) height image and (c') phase image.

The same sample was measured with different tips after careful
calibration for the tip radius for the cantilever deflection
sensitivity and also at different times. Additionally, the
piezoelectric z-axis was periodically calibrated with a known
depth grating.

PF-QNM is a contact AFM protocol based on the force−
volume method. Force−distance curves were recorded on a
point-by-point basis by means of the nanoindentation of the

sample. The piezoscanner was vibrated at 2 kHz while the
probe remained at rest. This provided a high-speed and
simultaneous acquisition of topographic images and force−
distance curves.[41,73−75] The maximum force (peak force) at
each pixel was controlled to obtain force−distance curves.
These force−distance curves were then used as a feedback
signal. By applying the DMT model, the analysis of the force−
distance curve was performed automatically by software and

allowed to extract the height, the elastic modulus, the adhesion force, the deformation, and the dissipation simultaneously.

2.4.5. Vulcanization Process. The curing behavior was analyzed at 160 °C by applying a deformation of 6.98% at a frequency of 1.667 Hz using a Rubber Process Analyzer, RPA 2000 from α Technologies (Wiltshire, U.K.). After, each compound was vulcanized in a hydraulic press under pressure at the same temperature using the optimum cure, t_{97} (time to reach 97% conversion) was determined with the RPA analyzer.

2.4.6. Dynamical Mechanical Analysis. Using a TA Q8000 dynamic mechanical analyzer (TA Instruments, Inc.), in tension mode at a 10 Hz frequency, the Payne effect was investigated by measuring the storage modulus (G') and the loss modulus (G'') at different shear strain amplitudes (0.04–60%) at 40 °C on vulcanized dumbbell geometry samples according to ASTM D638 with a 1 mm thickness.

2.4.7. Mechanical Properties. Tensile test experiments were done with a universal mechanical tester (Instron 3366 series, Norwood, MA). For each compound, five specimens were tested with a crosshead speed of 500 mm/min strain rate, according to the ISO 37 (die type 2) standard.

3. RESULTS AND DISCUSSION

3.1. Morphology and State of Carbon Nanotube Dispersion.
In order to obtain a deep understanding of the properties of CNT/rubber compounds, it is important to perform a precise characterization of the morphology of these particles, as well as their degree of dispersion when added to the elastomeric matrix and the CNT surface–rubber interaction. It is widely reported in the literature that these factors have a strong effect on the in-rubber properties.[22,76] In this work, field emission scanning electron microscopy (FESEM) was used to characterize the morphology of CNTs. Figure 1 shows the images obtained and their diameter histograms of pristine (a) and functionalized CNTs ((b) CCNT and (c) for TCNT). The characteristic tubular morphology of CNTs, which is maintained after the oxidative-sulfur functionalization process of the particles, as well as the typical rolled-up spherical morphology can be clearly observed.

To determine how the oxidative-sulfur-functionalizing procedures affected the structure of the CNT, the diameters of the tubes were calculated by analyzing different SEM images using ImageJ software. The diameter distributions of the CNTs present some differences. The average diameter of pristine samples is in the order of 14.3 ± 4.7 nm, whereas the oxidative-sulfur functionalization treatment affects the average diameters of particles. Both CCNT and TCNT present mean diameters lower than those of pristine CNTs as a result of the oxidation step in the modification process, being smaller in the case of CCNT (12.7 ± 4.6 nm). The acid treatment is more aggressive than the thermal one, and as a consequence, the morphology of the particles is affected to a higher degree, as can be observed by the average diameter measured. Diameters are similar to other values obtained from the literature.[19,41]

As it was described in detail in previous work,[39] the deconvolution C 1s and S 2p X-ray photoelectron spectroscopy (XPS) spectra were used to analyze the chemical bonding of different moieties during the CNT functionalization process. Hence, a single peak at 284.6 eV, assigned to the sp^2 C–C bonds of graphitic carbon, dominates the C 1s spectrum of pristine CNTs. In the case of modified nanotubes, a peak at 286 eV has been detected, and this peak is assigned to the C–S

bond. This grafted sulfur is able to react during the vulcanization process with the rubber chains, improving the rubber–filler interfacial interactions.

The dispersion of the different MWCNTs in the rubber matrix was analyzed by tapping mode AFM images. Both topography and phase images are shown in Figure 2. While the surface roughness[11] is revealed by the height signal, the phase angle difference between the excitation signal and the cantilever response identifies regions with different stiffness[2,13,20,77] and provides information about the shape and size of local heterogeneities at the nanometer scale.

The height signal reveals surface roughness, while the measurement of the difference between the phase angle of the excitation signal and the phase angle of the cantilever response gives information about the size and shape of local heterogeneities at the nanometric scale, identifying regions with different stiffness.[2,13,20,77] Hence, the brighter zones in the phase images obtained with moderate tapping (see Figure 2a′–c′) correspond to the zone in which CNTs are present.

During mixing, the shear stress causes the compounds to suffer great deformations when they are passed between the rolls, just after the rubber immediately recovers this shape. These two processes (distortion and recovery) occur many times and compete with the interactions between the nanotubes.[78] This results in a dispersion of isolated and agglomerated nanotubes in the matrix. Every compound shows some micrometer-scale agglomerates and some isolated nanotubes.

Comparing the three-phase images, it is observed that SBR-UCNT shows a higher fraction of CNTs on the surface. In addition, these unmodified CNTs seem to be longer than modified CNTs. A possible explanation is that the shear stress will be capable of overcoming the electrostatic and van der Waals interactions between these nanotubes.

However, nanotubes from oxidation treatments were more entangled, creating bigger agglomerates; this effect is more noticeable in the case of CNTs from chemical oxidation. Also, isolated CCNTs seem smaller and more isolated than the others, as explained above, which could be due to the more aggressive acid treatment that provokes the shortening or breaking of the nanotubes. The shortening causes a decrease in the high aspect ratio, which is one of the potential advantages of the use of CNTs as a reinforcement fiber.[13] Additionally, the presence of elemental sulfur and oxygen-bearing groups on the surface of modified CNTs was confirmed in our previous work based on thermogravimetric analysis and X-ray photoelectron analysis.[39] Thermogravimetric analysis of functionalized CNTs shows a significant weight loss in the range of temperatures between 150 and 350 °C. Comparing the TGA curves from functionalized CNTs with the TGA curve of elemental sulfur, this loss is attributed to the sulfur functional groups bonded to the CNT surface.

Due to the difficulty in obtaining good topographic images of rubber/CNT compounds,[13,22] roughness analysis of the three compounds was carried out. Roughness analysis is usually displayed by two parameters named R_a and R_q.[68] As the roughness analysis is based on the vertical axis, the topographic height images are used in this work. Considering that fillers are highly irregular particles of different sizes, the surfaces of these samples are randomly roughened, as shown in the R_q and R_a values of Table 1.

Both R_q and R_a show that the unmodified sample has the highest roughness, and the R_q of SBR-UCNT is similar to

Table 1. Root-Mean-Square Average (R_q) and Average Roughness (R_a) of SBR-UCNT, SBR-CCNT, and SBR-TCNT Compounds

samples (5 μm $\times$ 5 μm)	R_q (nm)	R_a (nm)	$R_q - R_a$ (nm)
SBR-UCNT	53.0 ± 0.9	42.0 ± 0.9	11.0 ± 0.1
SBR-CCNT	37.9 ± 1.7	28.3 ± 1.2	9.6 ± 0.5
SBR-TCNT	15.7 ± 0.9	11.4 ± 0.7	4.3 ± 0.2

others obtained from the literature.[11] Taking into account that the difference between R_q and R_a is indicative of the presence of filler particles in the surface,[79] $R_q - R_a$ of the three composites were calculated. Hence, the greater $R_q - R_a$ value corresponds to the SBR-UCNT composite; in contrast, the lowest value corresponds to the SBR-TCNT composite. However, the RMS roughness analysis provides only primary information about the fine-scale variations in the effective surface height, as this analysis does not show the lateral spacing of the surface feature.

In this framework, power spectral density (PSD) analysis was used to evaluate both the height deviation of the roughness profile and its lateral distribution.[79] Surfaces are considered as a superposition of spatial waves in the context of PSD.[77] Fourier transform (used to correlate real space with frequency space) allows measurement of the variation of height in real space in terms of the power spectrum in frequency space. Hence, any instrument's surface data can be viewed as a series of height values corresponding to spatial positions. Figure 3 shows the total power equivalent RMS (square root of the total power values) obtained from the power spectral density analysis.

The intensity of spectral spikes is much higher in the samples filled with pristine CNTs, indicating a higher roughness surface in this compound. The smaller intensity of the spikes is shown by the compound with CCNTs, supporting the results obtained for the total power and equivalent RMS.

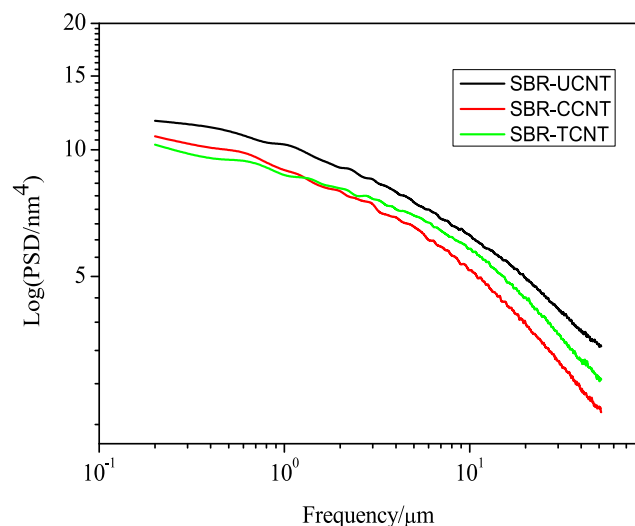|	SBR-UCNT	SBR-CCNT	SBR-TCNT
Total power, nm^2	2810±302	222±38	173±4
Equivalent RMS, nm	53.0±3.0	14.9±0.9	13.1±0.5

Figure 3. Plot of two-dimensional power spectral density vs spatial frequency of the three composites.

Observing the results of the power spectral analysis, the higher presence of particles on the surface of the SBR-UCNT compound is confirmed, as observed by either height images or R_q and R_a values.

Therefore, the oxidative-sulfur functionalization procedures of the carbon nanotubes provoke (i) a slight decrease in the diameter of the CNTs, (ii) a shortening of the overall length of the tubes, and (iii) modification of the chemical nature of the particles surface.[80] This modification improves the CNT-SBR interactions by means of introducing some active groups on the surface of nanotubes, so covalent bonds are created between CNTs and the rubber matrix; as a consequence, the presence of CNTs on the surface of these composites is minor compared to unmodified CNT where the filler−rubber interactions are weaker. As a result of the weak forces between CNTs, such as van der Waals and $\pi-\pi$ interactions, CNTs tend to become entangled with each other, forming large agglomerates known as bundles.[39] In addition, differences between the two oxidative-sulfur functionalization processes have been observed. In the case of SBR-CCNT, agglomerates are bigger than SBR-TCNT because the more aggressive oxidation treatment provokes structural damage as a consequence of the treatment with strong acids,[63] so the shape of these agglomerates lose the typical shape of CNT, as shown in Figure 2b′. The profile of SBR-CCNT also points out the minor presence of nanotubes at the surface. In contrast, SBR-TCNT shows fewer agglomerates as well as maintains its appearance like needles, as shown in Figure 2c′. This result agrees with those obtained in the roughness analysis. In addition, the modification of the particles can produce some changes in the vulcanization process. These effects will be studied further in Section 3.4 of this paper.

As SBR is an insulator, the addition of conductive particles as carbon nanotubes improves the electrical conductivity of this matrix. Every compound used in this study has the same amount of CNTs (10 phr), and this volume filler is above the percolating threshold in the case of unmodified nanotubes, such as shown in previous work.[25] In this framework, another approach to evaluate the dispersion of the nanotubes in the three different composites is electric force microscopy measurements (EFM). The long-range electrostatic forces shift the resonance frequency of the oscillating cantilever during EFM measurements. By monitoring changes in the phase shift of the electrostatic force gradient, changes in the cantilever resonant frequency due to the presence of a force gradient are detected.[81] The bright contrast in the EFM images (Figure 4) corresponds to a positive phase shift or an increase in the resonance frequency, which reflects the repulsive interaction between the cantilever and the sample. However, the attractive forces provoke a reduction in the frequency of the cantilever, and this effect is observed for a negative phase shift in the electrostatic force gradient image.[67] The image derived from the current map was quite suitable for depicting the dispersion of CNTs in an elastomeric polymer system because higher currents tunnel when the tip scans the CNTs, while lower currents pass when the tip scans the polymer.[20,40]

Both SBR-UCNT and SBR-TCNT compounds exhibit a number of localized higher insulating regions surrounded by lower conductive regions (bright). The increase of the bias voltage provokes the bright zones to show more contrast compared to the insulating regions recorded at the same biases. This result is in agreement with the images reported in the
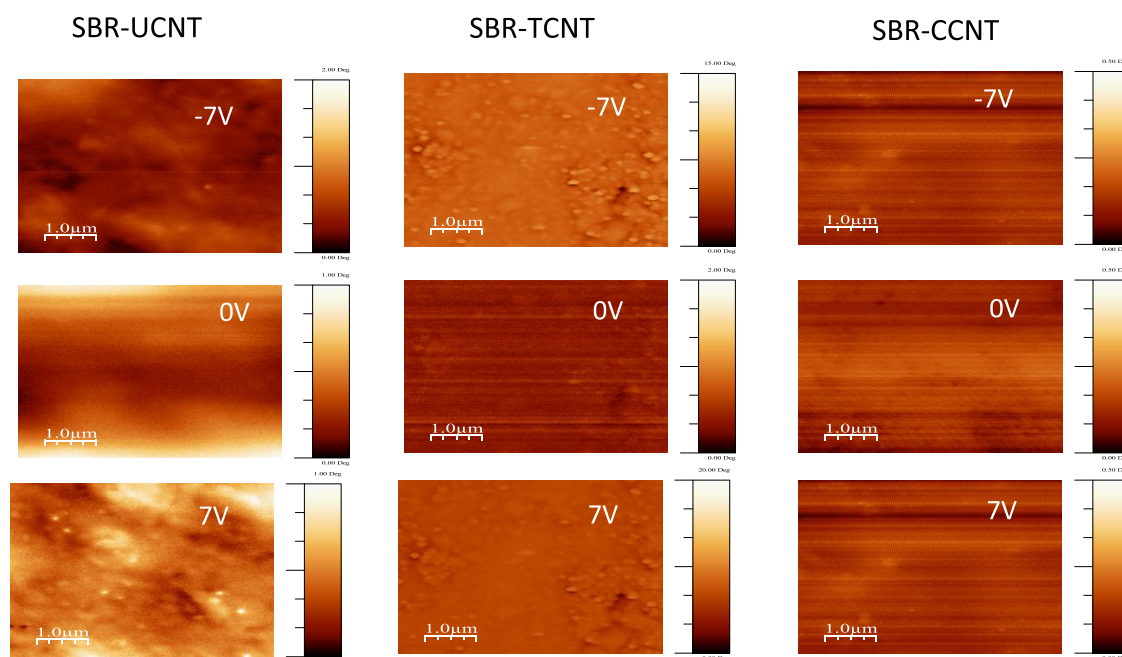
SBR-UCNT   SBR-TCNT   SBR-CCNT

Figure 4. EFM phase images of the three composites obtained by varying the bias from a negative to a positive value passing through 0 V.
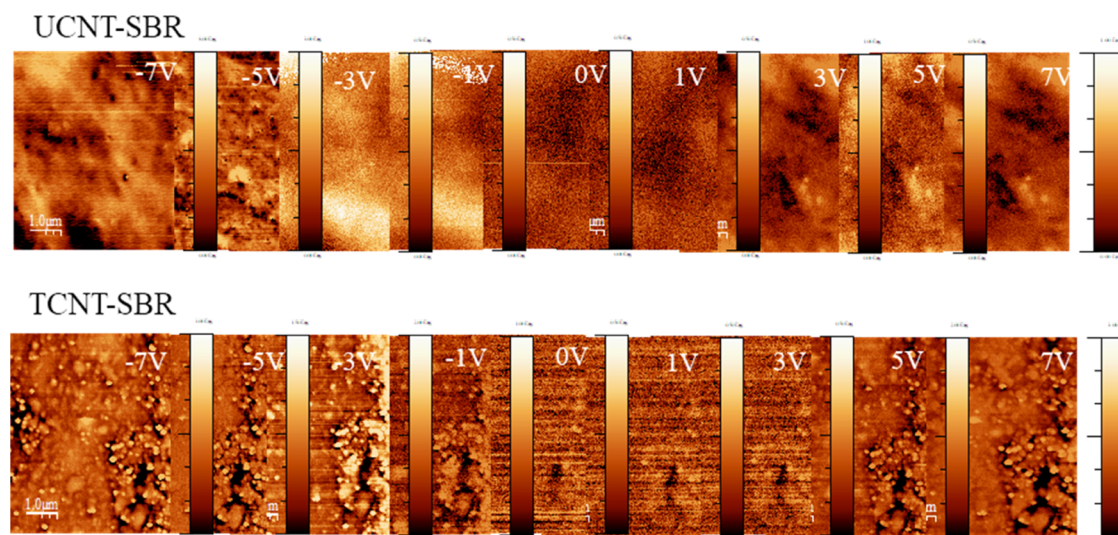

Figure 5. EFM phase images of UCNT-SBR and TCNT-SBR composites obtained by varying the bias from a negative to a positive value passing through 0 V.

literature.[40] The scene is completely different in the case of the SBR-CCNT.

The SBR-CCNT composite shows a higher number of insulating regions, and the bright regions of this composite do not depend on the sign of the bias applied. This fact could be due to the reduction of the aspect ratio as a consequence of the chemical oxidation (these nanotubes are more agglomerated in the rubber matrix), which decreases the particle−particle contact, reducing the electrical conductivity, as well as the surface modification disturbs the π-electron system of these particles, reducing the electrical conductivity properties of pristine CNTs.[11,39,82]

Both SBR-UCNT and SBR-TCNT show similar behaviors when the voltage of the tip is changed (Figure 5). When the negative shift increases, the bright zones increase, reflecting the attractive interaction between the cantilever and the speci-

men.[67] This result is in agreement with the ones reported in the literature.[40]

By means of EFM measurements, the greatest presence of nanotubes on the surface of the SBR-UCNT compound and the combination of bright zones with isolated nanotubes and agglomerated nanotubes in the two composites is confirmed, which are in accordance with the results obtained by tapping mode AFM (see Figure 5 SBR-UCNT, −5 V and SBR-TCNT −5 V).

3.2. Quantitative Analysis of the Interphase by the AFM PF-QNM Technique. PF-QNM AFM was used to quantitatively measure the nanomechanical properties of the three composites. Height, Young's modulus, adhesion energy, and deformation images of the three composites were acquired simultaneously in a single scan and at the same point. Thus, regions with a high elastic modulus, low adhesion energy, and
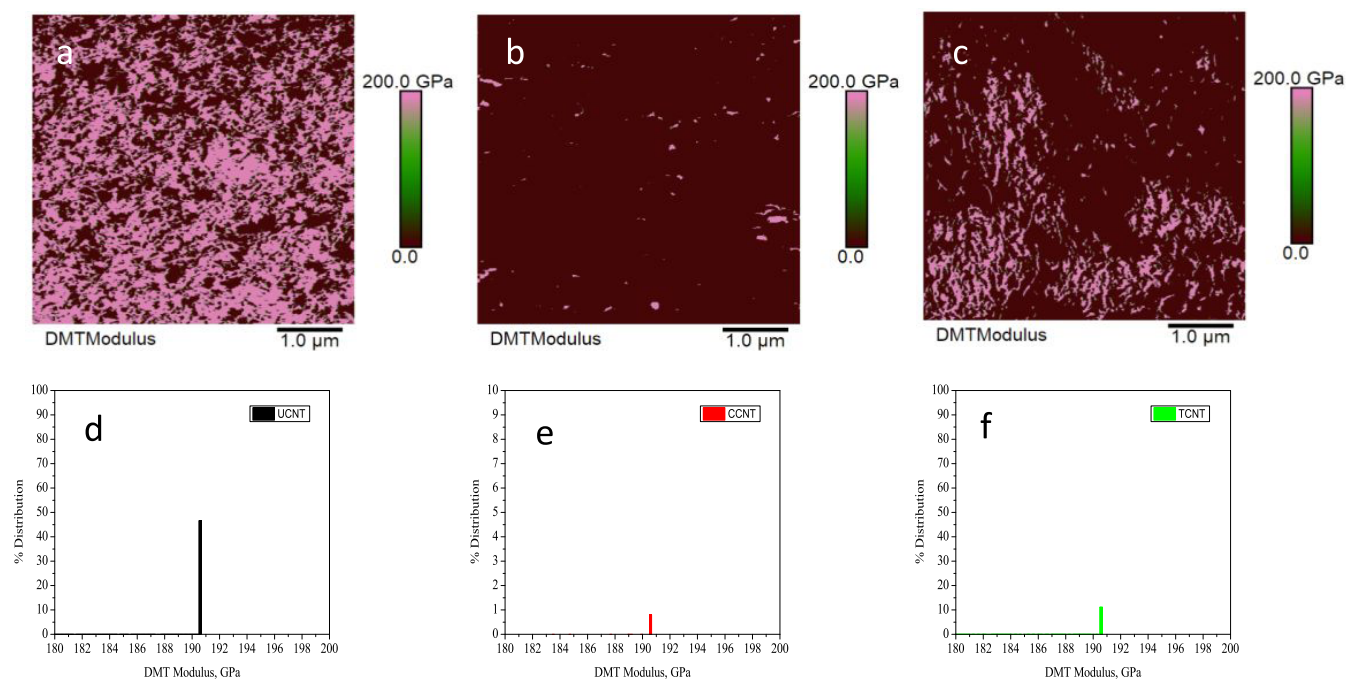
Figure 6. (a−c) DMT modulus images of UCNT-SBR, CCNT-SBR, and TCNT-SBR, respectively. (d−f) % CNT on the surface measured by the DMT modulus of the three composites at a high modulus (around 190 GPa).

low deformation correspond to CNTs, and regions with a low elastic modulus, high adhesion, and high deformation correspond to rubber.

Comparing the DMT modulus of these three composites, clearly different behaviors are observed. So, SBR-UCNT shows about a 46% high modulus (around 190 GPa), which corresponds to the CNT in the surface, while only 0.7% is observed in the case of SBR-CCNT, and around 11% in the case of SBR-TCNT. These results are in accordance with previous results obtained based on tapping AFM and EFM and allow us to determine quantitatively the proportion of CNTs on the surface, as shown in Figure 6.

To conclude the characterization of these three composites on a nanometric scale, the characterization of the interphase between CNT and rubber was carried out by means of the AFM PF-QNM technique. So, to choose the appropriate region for studying the interphase, two force−distance curves were acquired: one for one isolated CNT and another for the matrix because the mechanical responses of CNTs and rubber are very different.

While CNT is one of the most stiffness materials, the long-range elasticity is the main characteristic of SBR as a consequence of its elastomeric nature;[83,84] as a result, the interaction between the tip and the material is very distinct, as shown in Figure 7. In the case of the force−distance curve of CNT, the shape of the curve corresponds to a rigid material as expected; CNT shows a fiber-like structure, whereas the SBR matrix shows the behavior of elastic materials, as it was commented previously.

Another key factor to study the interphase is the election of the appropriate CNT for two reasons: On the one hand, only CNTs isolated were chosen because the real interphase thickness between CNT aggregates and rubber is inaccurate as a consequence of the presence of other CNTs,[75] and on the other hand, every CNT selected in all three composites showed a high modulus, low adhesion, and low deformation
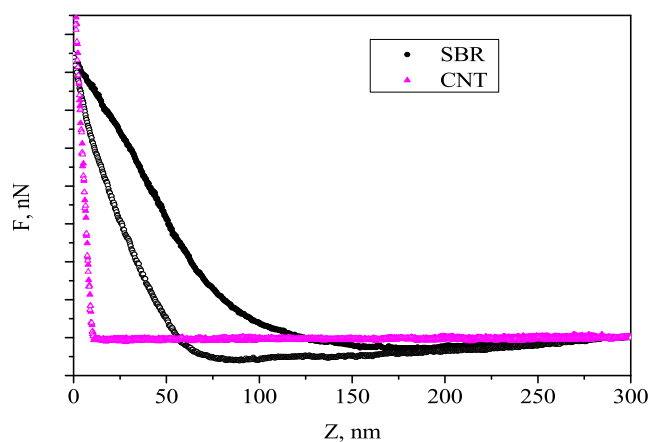

Figure 7. Qualitative comparative analysis of the force−distance curve of the CNT and the SBR matrix measured in the same form.

because these regions correspond to CNTs close to the sample surface, with the aim to avoid CNTs covered by a polymer,[41] at least in a small part of the CNT for these measures. Basically, the interphase is the region between the filler and rubber, where the chain mobility of the polymer is restricted by the presence of the filler; as a result, the stiffness in this region is higher than in the rubber region.[41,61,75] Taking this into account, the change in the modulus and adhesion force can be used to calculate the thickness of the interphase layer, as described by Ning et al. in their method.[41] Hence, profiles of the height, DMT moduli, and adhesion of each kind of CNT were measured in 10 different nanotubes; results from these measures were used to check the thickness of the interphase in the three composites. Both the adhesion force−width curve and moduli show a gradient change from the rubber to CNT in the three composites. In the case of the adhesion force−width curve, the highest values in the case of the rubber zone to minimum values as a consequence of the presence of CNT are
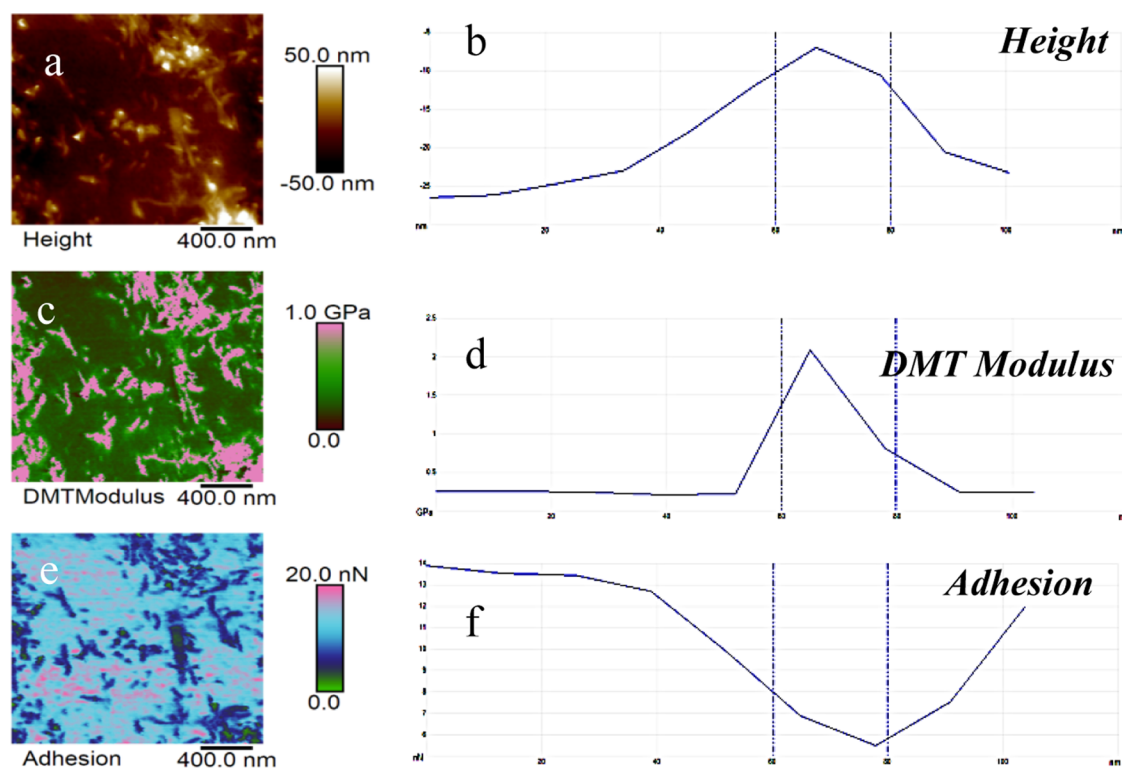
Figure 8. Representative (a) height image, (c) DMT modulus image, and (e) adhesion image of TCNT composites. (b) Corresponding height–width curve, (d) corresponding DMT modulus–width curve, and (f) adhesion–width curve obtained from the appropriate position of images.
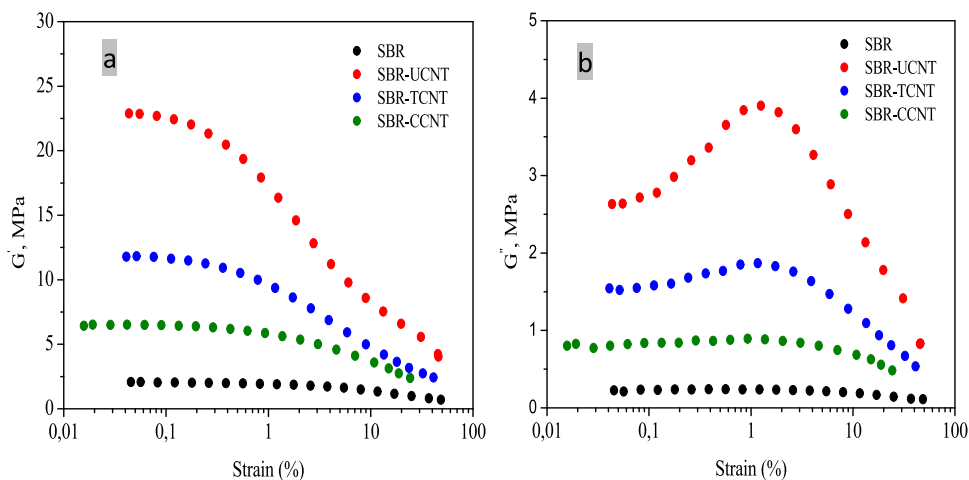

Figure 9. (a) Strain dependence of the storage modulus, G', at 40 °C for the studied rubber compounds. (b) Strain dependence of the loss modulus, G'', at 40 °C for the studied rubber compounds.

observed; in contrast, moduli vary from minimum values to highest values in the CNT.

Figure 8 shows the height–width curve (b), modulus–width curve (d), and adhesion force–width curve (f) directly obtained by computer software of AFM in the TCNT composite as an example of profiles used to compare the interphase thickness of the three composites. Thus, the corresponding length of the interfacial region on the horizontal curve minus the diameter of the CNTs calculated by the height image represents the estimated thickness of the interfacial layer of the three composites. The diameters obtained from the height image obtained at the same time that moduli and adhesion force images are 12.0 ± 3.5 nm in the UCNT

composite, 11.2 ± 0.6 nm in the CCNT composite, and 10.3 ± 1.1 in the TCNT composite.

The diameter of unmodified CNTs is higher than modified CNTs because the oxidative-sulfur functionalization affects the average diameters of particles, as commented previously (Figure 1). Thus, the corresponding estimated length of the interfacial region on the horizontal curves of DMT moduli and adhesion force curves minus the diameter of the CNTs represents the thickness of the interfacial layer. Results demonstrate that the average interfacial thickness of the UCNT composite is between 11.7 and 10.6 nm, whereas the interfacial thickness of the CCNT composite is between 10 and 9.8 nm and 12.5 and 10.3 in the case of the TCNT composite.

Therefore, the thickness of the interfacial layer calculated in the present study by the PF-QNM AFM technique is similar to a CNT elastomer composite[41,57] and a carbon black elastomer composite (10 nm)[45] reported in previous studies. Therefore, the oxidative-sulfur functionalization of the carbon nanotubes not only provokes changes in the diameter and shortening of the overall length CNTs, but additionally, the modification of the chemical nature of the particle surface produces changes in the nature of filler−rubber interactions; hence, the TCNT composite shows the thicker interfacial thickness, which could indicate stronger interaction between the filler and the rubber matrix.

Considering nanometric results, the second part of this paper is based on macroscale analysis with the aim of understanding the reinforcement produced by these three different CNTs and their effect on the composite. Thus, the interfacial interaction between CNTs and the SBR matrix by measuring dynamic mechanical properties was studied. In addition, the vulcanization curves and mechanical properties of the composites were further studied.

3.3. Payne Effect of Vulcanized SBR/CNTs.
The influence of the nanofillers on the dynamic behavior of these vulcanizates was studied by strain−sweep experiments. Figure 9a,b shows the variation of the storage modulus, G', and the loss modulus, G'', respectively. While the storage modulus remains constant in the unfilled compounds, it decreases in the filled compounds as the applied deformation increases. This effect is called the Payne effect and is attributed to the rupture of the filler network, which provokes the release of the polymer trapped in filler aggregates, as well as rubber−filler bonding and debonding mechanisms.[39,85−87] The higher the G' at the initial strain G'_0 and $\Delta G'$ (the difference between G'_0 and the ultimate dynamic storage modulus at high strains, G'_∞), the stronger the filler−filler networks, Therefore, important differences in the filler network and/or the rubber fraction influenced by the presence of filler aggregates are responsible for the abrupt reduction of the Payne effect in modified CNT composites, especially in the case of CCNT composites compared to unmodified CNT composites. So, the agglomerates formed during the chemical modification process cannot be broken with the applied strain. This is confirmed when analyzing the behavior of G''.

Thus, due to the agglomeration of CNT particles during the oxidation treatment, the behavior of SBR-CCNTs is strongly influenced by the poorer filler dispersion, as observed by SEM and phase images of tapping mode AFM, EFM, and PF-QNM AFM previously described in this work. Although this effect is more pronounced in the case of chemical treatment, it also occurs during the thermal one. For this reason, SBR-UCNT shows a higher G'_0 and Δ_G' when compared with the samples containing modified CNTs. However, nanoscale results indicate the stronger interaction between TCNT and the SBR matrix.

In agreement with these results, the difference between the loss moduli $G^{\wedge''}$, obtained at the minimum and maximum strain $\Delta G^{\wedge''}$, which is correlated to the energy dissipation associated with the filler−rubber−filler interactions, shows the same behavior. The modified nanoparticles created covalent bonds among themselves, which increased the resistance of the CNT aggregates to breakage during rubber deformation and diminished the energy dissipation phenomena associated with the breakage. These results are in concordance with previous studies based on NR-CNT composites.[39]

3.4. Vulcanization Process of Rubber Compounds.
Another aspect to consider is the effect of CNT in the vulcanization process due to two factors: on the one hand, the effect of CNT in the torque response due to the reinforcement effect of CNTs, and on the other hand, the presence of sulfur on the surface of modified CNTs. This fact leads to changes in the vulcanization curves, as shown in Figure 10. Curing agents
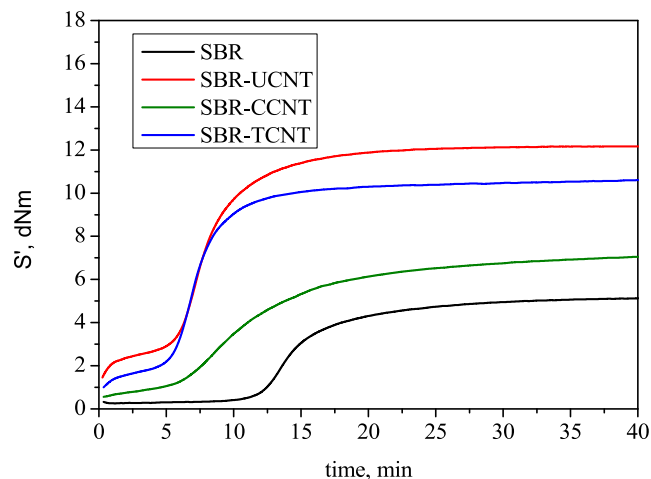

Figure 10. Rheometer curves of the nanocomposites.

must dissolve in the rubber and diffuse to the active sites in order to react effectively for efficient cross-linking of the rubber.[88] All composites have the same recipe, maintaining the amount of sulfur in 1 phr, either inserted on the CNT or added externally. The reinforcing effect of CNTs causes a notable increase in torque for SBR-CNT composites compared to that of the unfilled sample.

The modification of CNTs has a great influence on the cure kinetics by reducing the torque value because one part of the whole amount of sulfur is anchored to the surface of CNTs by a covalent bond in the case of modified CNTs, so this sulfur hinders the diffusion in the rubber matrix; as a consequence of the strong interactions between nanotubes, the result is that the torque value reduces, and this effect is more pronounced in the case of the SBR-CCNT composite because this oxidation leads to the formation of acidic groups, produced by the treatment with nitric and sulfuric acid. This behavior observed can be explained by a poor purification of CCNT after the acid treatment of the particles; NO_3^- and SO_4^{2-} could remain at the CNT surface, which provokes the absorption of basic accelerators, which decreases the vulcanization degree. As a consequence, a deceleration of the cure reaction and a relatively low final torque level are obtained, which leads to lower values of cross-link density and, therefore, a deterioration of the final properties of this compound.

The increase in the minimum torque, S'_{min}, observed in the modified CNTs is related to the viscosity of the compound. When CNTs are added to the rubber matrix, a strong filler network is formed, and consequently, the viscosity increases. As can be observed, the SBR-CCNT compound has a lower S'_{min}. This could indicate that this sample presents a lower degree of a filler network because the process reduces its aspect ratio. Therefore, the particle−particle contact is more difficult.

The torque increase ($\Delta S' = S'_{max} - S'_{min}$) is associated with the cross-link density of the compounds. As expected, the torque increase shows an increase with CNTs added; this

tendency is more pronounced in the case of SBR-UCNT; therefore, the samples with surface-modified particles could have lower values of cross-link density.[89−91]

3.5. Mechanical Properties of Vulcanized SBR/CNTs.

Finally, the results of the mechanical properties are illustrated in Figure 11. Results indicate the improvement in tensile
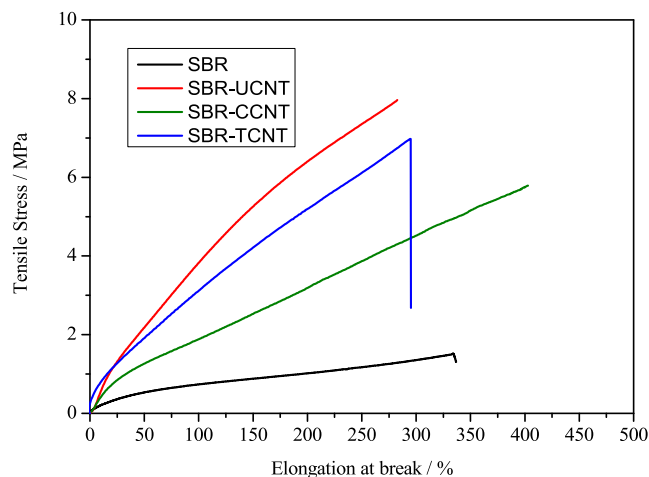

Figure 11. Mechanical properties of the three composites compare to a pure SBR compound.

strength with the CNT composite compared with unloading SBR. Concerning the three composites with CNTs, the trend is the same as observed by other techniques; the SBR-CCNT composite shows less tensile strength and more elongation at break than the others as a consequence of the more aggressive treatment, which provokes shortening and breaking of these CNTs in some way, as well as the poorer filler dispersion. In the case of SBR-TCNT also, agglomerates and aggregates are created during the thermal oxidation. Although the dispersion and the rubber−filler interaction in the case of the SBR-TCNT sample are better than those in the unmodified nanotubes, they are not sufficient to counteract the strong filler−filler interaction due to the covalent bonds created between the nanotubes during the oxidation treatment and form large aggregates and agglomerates that cannot be broken during mixing.

4. CONCLUSIONS

In spite of the excellent and promising properties of CNT as a nanofiller, its use is limited by achieving a good dispersion into the elastomer matrix, which is a key factor in the reinforcement of this nanocomposite. In this sense, the current study is based on nanoscale characterization by three different techniques based on atomic force microscopy (TM-AFM, EFM and PF-QNM-AFM) with the purpose of studying in-depth the dispersion of both unmodified and two types of sulfur-modified CNTs into an SBR matrix and the interphase rubber−filler.

- The oxidizing-sulfur functionalizing process does not modify the tubular morphology of the particles. However, the average diameter of nanotubes decreases as a consequence of the oxidative-sulfur functionalization process; this effect is more pronounced in the case of acid treatment, as shown by FESEM images and height images of PF-QNM AFM measures.

- Although height and phase images of tapping mode show isolated and agglomerates of CNTs, the proportion of agglomerates is very different in the three nano-composites. So, the SBR-CCNT composite shows the smallest isolated nanotubes in combination with great zones of aggregates. This fact could be due to the more aggressive acid treatment provoking the shortening or breaking of the nanotubes. The shortening causes a decrease in the high aspect ratio, which is one of the potential advantages of its use as a reinforcement fiber.

- Either the greater value of $R_q−R_a$ or the highest RMS obtained by power spectral analysis is indicative of the most presence of filler particles on the surface. This result is quantified and confirmed by DMT moduli PF-QNM AFM measures. Hence, only around 1% CCNT is on the surface of SBR-CCNT, around 11% in the case of SBR-TCNT, and around 46% in the case of SBR-UCNT. Also, the EFM measure confirmed the greatest presence of nanotubes on the surface of the SBR-UCNT compound. In contrast, the SBR-CCNT composite shows a higher number of insulating regions, which confirms the results obtained by AFM analysis.

- By using the AFM PF-QNM technique, it is possible to compare the interfacial layer thickness of CNTs-SBR composites using the method developed by Ning.[41] Results demonstrate that the average interfacial thickness of the UCNT composite is between 11.7 and 10.6 nm, whereas the interfacial thickness of the CCNT composite is between 10 and 9.8 nm and 12.5 and 10.3 in the case of the TCNT composite. Therefore, the oxidizing-sulfur functionalizing process of the carbon nanotubes also produces changes in the nature of filler−rubber interactions; hence, the TCNT composite shows a thicker interfacial thickness, which could indicate the stronger interaction between the filler and the rubber matrix.

- This work has shown that the macroscopic behavior of these materials, such as mechanical properties, must be related to phenomena that occur at different length scales and are visible using different techniques. At the nanoscale, it is possible to study the rubber−filler interaction as well as the dispersion of the nanoparticles in the matrix. At the mesoscale, such as the Payne effect, the effect of the filler network and the formation of agglomerates of micrometric size predominate.

■ AUTHOR INFORMATION

Corresponding Author

Pilar Posadas − Instituto de Ciencia y Tecnología de Polímeros (CSIC), 28006 Madrid, Spain; ⊙ orcid.org/0000-0003-4137-9689; Email: pposadas@ictp.csic.es

Authors

Pilar Bernal-Ortega − Department of Mechanics of Solids, Surfaces & Systems (MS3), Chair of Elastomer Technology & Engineering, Faculty of Engineering Technology, University of Twente, 7500 AE Enschede, The Netherlands; ⊙ orcid.org/0000-0002-1305-3000

M. Mar Bernal − Dipartimento di Scienza Applicata e Tecnologia, Politecnico di Torino, 15121 Alessandria, Italy

Aurora Nogales − Instituto de Estructura de la Materia, IEM-CSIC, 28006 Madrid, Spain; ⊙ orcid.org/0000-0002-2494-3551

Rodrigo Navarro − *Instituto de Ciencia y Tecnología de Polímeros (CSIC), 28006 Madrid, Spain;* ⊙ orcid.org/0000-0001-6592-9871

Juan L. Valentín − *Instituto de Ciencia y Tecnología de Polímeros (CSIC), 28006 Madrid, Spain;* ⊙ orcid.org/0000-0002-3916-9060

Complete contact information is available at:
https://pubs.acs.org/10.1021/acsomega.4c02163

Notes

The authors declare no competing financial interest.

■ REFERENCES

(1) Clément, F.; Lapra, A.; Bokobza, L.; Monnerie, L.; Ménez, P. Atomic Force Microscopy Investigation of Filled Elastomers and Comparison with Transmission Electron Microscopy - Application to Silica-Filled Silicone Elastomers. *Polymer* **2001**, *42* (14), 6259−6270.

(2) Špírková, M.; Pavličević, J.; Strachota, A.; Poreba, R.; Bera, O.; Kaprálková, L.; Baldrian, J.; Šlouf, M.; Lazić, N.; Budinski-Simendić, J. Novel Polycarbonate-Based Polyurethane Elastomers: Composition-Property Relationship. *Eur. Polym. J.* **2011**, *47*, 959−972.

(3) Zhou, X.; Zhu, Y.; Liang, J.; Yu, S. New Fabrication and Mechanical Properties of Styrene-Butadiene Rubber/Carbon Nanotubes Nanocomposite. *J. Mater. Sci. Technol.* **2010**, *26*, 1127−1132.

(4) Bertora, A.; Castellano, M.; Marsano, E.; Alessi, M.; Conzatti, L.; Stagnaro, P.; Colucci, G.; Priola, A.; Turturro, A. A New Modifier for Silica in Reinforcing SBR Elastomers for the Tyre Industry. *Macromol. Mater. Eng.* **2011**, *296* (5), 455−464.

(5) Ward, A. A.; Khalf, A. I. Electrical and Mechanical Properties of SBR Filled with Carbon Black-Silica Blends. *Kautsch. Gummi Kunstst.* **2007**, *60* (11), 623−630.

(6) Sae-Oui, P.; Suchiva, K.; Sirisinha, C.; Intiya, W.; Yodjun, P.; Thepsuwan, U. Effects of Blend Ratio and SBR Type on Properties of Carbon Black-Filled and Silica-Filled SBR/BR Tire Tread Compounds. *Adv. Mater. Sci. Eng.* **2017**, *2017*, No. 2476101.

(7) Bhattacharya, M.; Biswas, S.; Bhowmick, A. K. Permeation Characteristics and Modeling of Barrier Properties of Multifunctional Rubber Nanocomposites. *Polymer* **2011**, *52*, 1562−1576.

(8) Stephen, R.; Ranganathaiah, C.; Varghese, S.; Joseph, K.; Thomas, S. Gas Transport through Nano and Micro Composites of Natural Rubber (NR) and Their Blends with Carboxylated Styrene Butadiene Rubber (XSBR) Latex Membranes. *Polymer* **2006**, *47*, 858−870.

(9) Lu, Y. L.; Li, Z.; Yu, Z. Z.; Tian, M.; Zhang, L. Q.; Mai, Y. W. Microstructure and Properties of Highly Filled Rubber/Clay Nanocomposites Prepared by Melt Blending. *Compos. Sci. Technol.* **2007**, *67*, 2903−2913.

(10) Peddini, S. K.; Bosnyak, C. P.; Henderson, N. M.; Ellison, C. J.; Paul, D. R. Nanocomposites from Styrene-Butadiene Rubber (SBR) and Multiwall Carbon Nanotubes (MWCNT) Part 2: Mechanical Properties. *Polymer* **2015**, *56*, 443−451.

(11) Bokobza, L.; Bresson, B.; Garnaud, G.; Zhang, J. Mechanical and AFM Investigations of Elastomers Filled with Multiwall Carbon Nanotubes. *Compos. Interfaces* **2012**, *19* (5), 285−295.

(12) Bokobza, L.; Rapoport, O. Reinforcement of Natural Rubber. *J. Appl. Polym. Sci.* **2002**, *85* (11), 2301−2316.

(13) Bokobza, L. Multiwall Carbon Nanotube Elastomeric Composites: A Review. *Polymer* **2007**, *48*, 4907−4920.

(14) Chandra, C. S. J.; Shadiya, M. A.; Bipinbal, P. K.; Narayanankutty, S. K. Effect Of Olivine Nanosilica On The Reinforcement Of Natural Rubber Nanosilica Composites. *Mater. Today: Proc.* **2019**, *9*, 127−132.

(15) Hidayah, I. N.; Mariatti, M.; Ismail, H.; Kamarol, M. Evaluation of PP/EPDM Nanocomposites Filled with SiO2, TiO2 and ZnO Nanofillers as Thermoplastic Elastomeric Insulators. *Plast., Rubber Compos.* **2015**, *44* (7), 259−264.

(16) Chang, Y. W.; Lee, Y. Preparation and Properties of Polyethylene-Octene Elastomer (POE)/Organoclay Nanocomposites. *Polym. Bull.* **2012**, *68* (2), 483−492.

(17) Gauthier, C.; Chazeau, L.; Prasse, T.; Cavaille, J. Y. Reinforcement Effects of Vapour Grown Carbon Nanofibres as Fillers in Rubbery Matrices. *Compos. Sci. Technol.* **2005**, *65*, 335−343.

(18) Das, A.; Stöckelhuber, K. W.; Jurk, R.; Saphiannikova, M.; Fritzsche, J.; Lorenz, H.; Klüppel, M.; Heinrich, G. Modified and Unmodified Multiwalled Carbon Nanotubes in High Performance Solution-Styrene−Butadiene and Butadiene Rubber Blends. *Polymer* **2008**, *49* (24), 5276−5283.

(19) Peddini, S. K.; Bosnyak, C. P.; Henderson, N. M.; Ellison, C. J.; Paul, D. R. Nanocomposites from Styrene-Butadiene Rubber (SBR) and Multiwall Carbon Nanotubes (MWCNT) Part 1: Morphology and Rheology. *Polymer* **2014**, *55*, 258−270.

(20) Mensah, B.; Kim, H. G.; Lee, J. H.; Arepalli, S.; Nah, C. Carbon Nanotube-Reinforced Elastomeric Nanocomposites: A Review. *Int. J. Smart Nano Mater.* **2015**, *6* (4), 211−238.

(21) Junkong, P.; Kueseng, P.; Wirasate, S.; Huynh, C.; Rattanasom, N. Cut Growth and Abrasion Behaviour, and Morphology of Natural Rubber Filled with MWCNT and MWCNT/Carbon Black. *Polym. Test.* **2015**, *41*, 172−183.

(22) Das, A.; Stöckelhuber, K. W.; Jurk, R.; Fritzsche, J.; Klüppel, M.; Heinrich, G. Coupling Activity of Ionic Liquids between Diene Elastomers and Multi-Walled Carbon Nanotubes. *Carbon* **2009**, *47*, 3313−3321.

(23) Subramaniam, K.; Das, A.; Simon, F.; Heinrich, G. Networking of Ionic Liquid Modified CNTs in SSBR. *Eur. Polym. J.* **2013**, *49*, 345−352.

(24) Girun, N.; Ahmadun, F. R.; Rashid, S. A.; Atieh, M. A. Multi-Wall Carbon Nanotubes/Styrene Butadiene Rubber (SBR) Nanocomposite. *Fullerenes, Nanotubes Carbon Nanostruct.* **2007**, *15* (3), 207−214.

(25) Bernal-Ortega, P.; Bernal, M. M.; González-Jiménez, A.; Posadas, P.; Navarro, R.; Valentín, J. L. New Insight into Structure-Property Relationships of Natural Rubber and Styrene-Butadiene Rubber Nanocomposites Filled with MWCNT. *Polymer* **2020**, *201*, No. 122604.

(26) Avilés, F.; Cauich-Rodríguez, J. V.; Toro-Estay, P.; Yazdani-Pedram, M.; Aguilar-Bolados, H. Improving Carbon Nanotube/Polymer Interactions in Nanocomposites. In *Carbon Nanotube-Reinforced Polymers*; Elsevier, 2018; pp 83−115.

(27) Bai, L.; Bai, Y.; Zheng, J. Improving the Filler Dispersion and Performance of Silicone Rubber/Multi-Walled Carbon Nanotube Composites by Noncovalent Functionalization of Polymethylphenylsiloxane. *J. Mater. Sci.* **2017**, *52* (12), 7516−7529.

(28) Dyke, C. A.; Tour, J. M. Covalent Functionalization of Single-Walled Carbon Nanotubes for Materials Applications. *J. Phys. Chem. A* **2004**, *108* (51), 11151−11159.

(29) Karousis, N.; Tagmatarchis, N.; Tasis, D. Current Progress on the Chemical Modification of Carbon Nanotubes. *Chem. Rev.* **2010**, *110* (9), 5366−5397.

(30) Li, K.; Gu, B. Influence of Different Functionalization on Mechanical and Interface Behavior of MWCNTs/NBR Sealing Composites. *Mater. Res. Express* **2017**, *4* (4), No. 045303.

(31) Manna, R.; Srivastava, S. K. Fabrication of Functionalized Graphene Filled Carboxylated Nitrile Rubber Nanocomposites as Flexible Dielectric Materials. *Mater. Chem. Front.* **2017**, *1* (4), 780−788.

(32) Yan, J.; Liu, X.; Wang, X.; Li, B. Long-Life, High-Efficiency Lithium/Sulfur Batteries from Sulfurized Carbon Nanotube Cathodes. *J. Mater. Chem. A* **2015**, *3* (18), 10127−10133.

(33) Yuan, Z.; Peng, H. J.; Huang, J. Q.; Liu, X. Y.; Wang, D. W.; Cheng, X. B.; Zhang, Q. Hierarchical Free-Standing Carbon-Nanotube Paper Electrodes with Ultrahigh Sulfur-Loading for Lithium-Sulfur Batteries. *Adv. Funct. Mater.* **2014**, *24* (39), 6105−6112.

(34) Xu, T.; Yang, J.; Liu, J.; Fu, Q. Surface Modification of Multi-Walled Carbon Nanotubes by O 2 Plasma. *Appl. Surf. Sci.* **2007**, *253* (22), 8945−8951.

(35) Dementev, N.; Osswald, S.; Gogotsi, Y.; Borguet, E. Purification of Carbon Nanotubes by Dynamic Oxidation in Air. *J. Mater. Chem.* **2009**, *19* (42), 7904−7908.

(36) Datsyuk, V.; Kalyva, M.; Papagelis, K.; Parthenios, J.; Tasis, D.; Siokou, A.; Kallitsis, I.; Galiotis, C. Chemical Oxidation of Multiwalled Carbon Nanotubes. *Carbon* **2008**, *46* (6), 833−840.

(37) Balasubramanian, K.; Burghard, M. Chemically Functionalized Carbon Nanotubes. *Small* **2005**, *1* (2), 180−192.

(38) Velasco-Santos, C.; Martínez-Hernández, A. L.; Lozada-Cassou, M.; Alvarez-Castillo, A.; Castaño, V. M. Chemical Functionalization of Carbon Nanotubes through an Organosilane. *Nanotechnology* **2002**, *13* (4), 495−498.

(39) Bernal-Ortega, P.; Bernal, M. M.; Blume, A.; González-Jiménez, A.; Posadas, P.; Navarro, R.; Valentín, J. L. Sulfur-Modified Carbon Nanotubes for the Development of Advanced Elastomeric Materials. *Polymers* **2021**, *13* (5), No. 821.

(40) Peponi, L.; Tercjak, A.; Gutierrez, J.; Cardinali, M.; Mondragon, I.; Valentini, L.; Kenny, J. M. Mapping of Carbon Nanotubes in the Polystyrene Domains of a Polystyrene-b-Polyisoprene-b-Polystyrene Block Copolymer Matrix Using Electro-static Force Microscopy. *Carbon* **2010**, *48*, 2590−2595.

(41) Ning, N.; Mi, T.; Chu, G.; Zhang, L. Q.; Liu, L.; Tian, M.; Yu, H. T.; Lu, Y. L. A Quantitative Approach to Study the Interface of Carbon Nanotubes/Elastomer Nanocomposites. *Eur. Polym. J.* **2018**, *102*, 10−18.

(42) Le, H. H.; Parsaker, M.; Sriharish, M. N.; et al. Effect of Rubber Polarity on Selective Wetting of Carbon Nanotubes in Ternary Blends. *eXPRESS Polym. Lett.* **2015**, *9*, 960−971.

(43) Leblanc, J. L. Rubber-Filler Interactions and Rheological Properties in Filled Compounds. *Prog. Polym. Sci.* **2002**, *27* (4), 627−687.

(44) Papon, A.; Saalwächter, K.; Schäler, K.; Guy, L.; Lequeux, F.; Montes, H. Low-Field NMR Investigations of Nanocomposites: Polymer Dynamics and Network Effects. *Macromolecules* **2011**, *44* (4), 913−922.

(45) Qu, M.; Deng, F.; Kalkhoran, S. M.; Gouldstone, A.; Robisson, A.; Van Vliet, K. J. Nanoscale Visualization and Multiscale Mechanical Implications of Bound Rubber Interphases in Rubber-Carbon Black Nanocomposites. *Soft Matter* **2011**, *7* (3), 1066−1077.

(46) Nishi, T. Effect of Solvent and Carbon Black Species on the Rubber−carbon Black Interactions Studied by Pulsed NMR. *J. Polym. Sci., Polym. Phys. Ed.* **1974**, *12*, 685−693.

(47) Vidal, A.; Haidar, B. Soft Materials Filled Elastomers: Characteristics and Properties of Interfaces and Interphases, and Their Role in Reinforcement Processes. *Soft Mater.* **2007**, *5*, 155−167.

(48) Schneider, H.; Roos, M.; Golitsyn, Y.; Steiner, K.; Saalwächter, K. Dynamic Heterogeneity of Filler-Associated Interphases in Polymer Nanocomposites. *Macromol. Rapid Commun.* **2021**, *42* (11), No. 2100061.

(49) Goertzen, W. K.; Kessler, M. R. Dynamic Mechanical Analysis of Fumed Silica/Cyanate Ester Nanocomposites. *Composites, Part A* **2008**, *39* (5), 761−768.

(50) Fragiadakis, D.; Pissis, P. Glass Transition and Segmental Dynamics in Poly(Dimethylsiloxane)/Silica Nanocomposites Studied by Various Techniques. *J. Non-Cryst. Solids* **2007**, *353* (47−51), 4344−4352.

(51) Mensah, B.; Gupta, K. C.; Kim, H.; Wang, W.; Jeong, K. U.; Nah, C. Graphene-Reinforced Elastomeric Nanocomposites: A Review. *Polym. Test.* **2018**, *68*, 160−184.

(52) Das, C.; Bansod, N. D.; Kapgate, B. P.; Rajkumar, K.; Das, A. Incorporation of Titania Nanoparticles in Elastomer Matrix to Develop Highly Reinforced Multifunctional Solution Styrene Butadiene Rubber Composites. *Polymer* **2019**, *162*, 1−10.

(53) Pietrasik, J.; Gaca, M.; Zaborski, M.; Okrasa, L.; Boiteux, G.; Gain, O. Studies of Molecular Dynamics of Carboxylated Acrylonitrile-Butadiene Rubber Composites Containing in Situ Synthesized Silica Particles. *Eur. Polym. J.* **2009**, *45* (12), 3317−3325.

(54) Vo, L. T.; Anastasiadis, S. H.; Giannelis, E. P. Dielectric Study of Poly(Styrene-Co-Butadiene) Composites with Carbon Black, Silica, and Nanoclay. *Macromolecules* **2011**, *44* (15), 6162−6171.

(55) Tzounis, L.; Debnath, S.; Rooj, S.; Fischer, D.; Mäder, E.; Das, A.; Stamm, M.; Heinrich, G. High Performance Natural Rubber Composites with a Hierarchical Reinforcement Structure of Carbon Nanotube Modified Natural Fibers. *Mater. Des.* **2014**, *58*, 1−11.

(56) Abraham, J.; Thomas, J.; Kalarikkal, N.; George, S. C.; Thomas, S. Static and Dynamic Mechanical Characteristics of Ionic Liquid Modified MWCNT-SBR Composites: Theoretical Perspectives for the Nanoscale Reinforcement Mechanism. *J. Phys. Chem. B* **2018**, *122* (4), 1525−1536.

(57) Wang, D.; Fujinami, S.; Nakajima, K.; Niihara, K. I.; Inukai, S.; Ueki, H.; Magario, A.; Noguchi, T.; Endo, M.; Nishi, T. Production of a Cellular Structure in Carbon Nanotube/Natural Rubber Composites Revealed by Nanomechanical Mapping. *Carbon* **2010**, *48*, 3708−3714.

(58) Tadiello, L.; D'Arienzo, M.; Di Credico, B.; Hanel, T.; Matejka, L.; Mauri, M.; Morazzoni, F.; Simonutti, R.; Spirkova, M.; Scotti, R. The Filler-Rubber Interface in Styrene Butadiene Nanocomposites with Anisotropic Silica Particles: Morphology and Dynamic Properties. *Soft Matter* **2015**, *11* (20), 4022−4033.

(59) Frone, A. N.; Berlioz, S.; Chailan, J. F.; Panaitescu, D. M. Morphology and Thermal Properties of PLA-Cellulose Nanofibers Composites. *Carbohydr. Polym.* **2013**, *91* (1), 377−384.

(60) Martínez-Tong, D.; Najar, A. S.; Soccio, M.; Nogales, A.; Bitinis, N.; López-Manchado, M. A.; Ezquerra, T. A. Quantitative Mapping of Mechanical Properties in Polylactic Acid/Natural Rubber/Organoclay Bionanocomposites as Revealed by Nano-indentation with Atomic Force Microscopy. *Compos. Sci. Technol.* **2014**, *104*, 34−39.

(61) Smolyakov, G.; Pruvost, S.; Cardoso, L.; Alonso, B.; Belamie, E.; Duchet-Rumeau, J. AFM PeakForce QNM Mode: Evidencing Nanometre-Scale Mechanical Properties of Chitin-Silica Hybrid Nanocomposites. *Carbohydr. Polym.* **2016**, *151*, 373−380.

(62) Cohen-Karni, T.; Jeong, K. J.; Tsui, J. H.; Reznor, G.; Mustata, M.; Wanunu, M.; Graham, A.; Marks, C.; Bell, D. C.; Langer, R.; Kohane, D. S. Nanocomposite Gold-Silk Nanofibers. *Nano Lett.* **2012**, *12*, 5403−5406.

(63) Avilés, F.; Cauich-Rodríguez, J. V.; Moo-Tah, L.; May-Pat, A.; Vargas-Coronado, R. Evaluation of Mild Acid Oxidation Treatments for MWCNT Functionalization. *Carbon* **2009**, *47* (13), 2970−2975.

(64) Martínez, M. T.; Callejas, M. A.; Benito, A. M.; Cochet, M.; Seeger, T.; Ansón, A.; Schreiber, J.; Gordon, C.; Marhic, C.; Chauvet, O.; et al. Sensitivity of Single Wall Carbon Nanotubes to Oxidative Processing: Structural Modification, Intercalation and Functionalisation. *Carbon* **2003**, *41* (12), 2247−2256.

(65) Chiang, I. W.; Brinson, B. E.; Smalley, R. E.; Margrave, J. L.; Hauge, R. H. Purification and Characterization of Single-Wall Carbon Nanotubes. *J. Phys. Chem. B* **2001**, *105* (6), 1157−1161.

(66) Xu, M.; Sun, Z.; Chen, Q.; Tay, B. K. Effect of Chemical Oxidation on the Gas Sensing Properties of Multi-Walled Carbon Nanotubes. *Int. J. Nanotechnol.* **2009**, *6* (7−8), 735−744.

(67) Kim, J.; Jasper, W. J.; Hinestroza, J. P. Charge Characterization of an Electrically Charged Fiber via Electrostatic Force Microscopy. *J. Eng. Fibers Fabr.* **2006**, *1* (2), No. 155892500600100.

(68) Digital Instrument Veeco Nanoscope IVa Controller Manual Software Version 6.13, Chapter 4.

(69) He, C.; Hao, Y.; Zeng, H.; Tang, T.; Xing, J.; Chen, J. A New Purification Method for Carbon Nanotubes and Associated Atomic Force Microscope Force-Distance Curve Analysis. *Sep. Purif. Technol.* **2011**, *81*, 174−183.

(70) Koetniyom, W.; Suhatcho, T.; Treetong, A.; Thiwawong, T. AFM Force Distance Curve Measurement for Surface Investigation of Polymers Compound Blend with Metal Nanoparticles. *Mater. Today: Proc.* **2017**, *4* (5), 6205−6211.

(71) Wang, D.; Russell, T. P. Advances in Atomic Force Microscopy for Probing Polymer Structure and Properties. *Macromolecules* **2018**, *51*, 3−24.

(72) Derjaguin, B. V.; Muller, V. M.; Toporov, Y. P. Effect of Contact Deformations on the Adhesion of Particles. *J. Colloid Interface Sci.* **1975**, *53* (2), 314−326.

(73) Criado, M.; Rebollar, E.; Nogales, A.; Ezquerra, T. A.; Boulmedais, F.; Mijangos, C.; Hernández, R. Quantitative Nano-mechanical Properties of Multilayer Films Made of Polysaccharides through Spray Assisted Layer-by-Layer Assembly. *Biomacromolecules* **2017**, *18* (1), 169−177.

(74) Chyasnavichyus, M.; Young, S. L.; Tsukruk, V. V. Recent Advances in Micromechanical Characterization of Polymer, Bio-material, and Cell Surfaces with Atomic Force Microscopy. *Jpn. J. Appl. Phys.* **2015**, *54* (8), No. 08LA02.

(75) Tian, C.; Chu, G.; Feng, Y.; Lu, Y.; Miao, C.; Ning, N.; Zhang, L.; Tian, M. Quantitatively Identify and Understand the Interphase of SiO2/Rubber Nanocomposites by Using Nanomechanical Mapping Technique of AFM. *Compos. Sci. Technol.* **2019**, *170*, 1−6.

(76) Singh, V.; Joung, D.; Zhai, L.; Das, S.; Khondaker, S. I.; Seal, S. Graphene Based Materials: Past, Present and Future. *Prog. Mater. Sci.* **2011**, *56* (8), 1178−1271.

(77) Maiti, M.; Bhowmick, A. K. New Insights into Rubber-Clay Nanocomposites by AFM Imaging. *Polymer* **2006**, *47*, 6156−6166.

(78) Wang, D.; Fujinami, S.; Nakajima, K.; Inukai, S.; Ueki, H.; Magario, A.; Noguchi, T.; Endo, M.; Nishi, T. Visualization of Nanomechanical Mapping on Polymer Nanocomposites by AFM Force Measurement. *Polymer* **2010**, *51*, 2455−2459.

(79) George, S. C.; Rajan, R.; Aprem, A. S.; Thomas, S.; Kim, S. S. The Fabrication and Properties of Natural Rubber-Clay Nano-composites. *Polym. Test.* **2016**, *51*, 165−173.

(80) Bokobza, L. Enhanced Electrical and Mechanical Properties of Multiwall Carbon Nanotube Rubber Composites. *Polym. Adv. Technol.* **2012**, *23* (12), 1543−1549.

(81) Scanning Probe Microscopy and Spectroscopy: Theory, Techniques, and Applications *Choice Rev. Online* 2001; Vol. *38* 10, pp 38−5588 DOI: 10.5860/choice.38-5588.

(82) Endo, M.; Noguchi, T.; Ito, M.; Takeuchi, K.; Hayashi, T.; Kim, Y. A.; Wanibuchi, T.; Jinnai, H.; Terrones, M.; Dresselhaus, M. S. Extreme-Performance Rubber Nanocomposites for Probing and Excavating Deep Oil Resources Using Multi-Walled Carbon Nano-tubes. *Adv. Funct. Mater.* **2008**, *18* (21), 3403−3409.

(83) Treloar, L. R. G. The Structure and Mechanical Properties of Rubberlike Materials. In *Theorie und Molekulare Deutung Technolo-gischer Eigenschaften von Hochpolymeren Werkstoffen*; Springer : Berlin Heidelberg, 1975.

(84) Erman, B.; Mark, J. E.*Structures and Properties of Rubberlike Networks*; Oxford University Press, 1997.

(85) Bandzierz, K.; Reuvekamp, L.; Dryzek, J.; Dierkes, W.; Blume, A.; Bielinski, D. Materials Influence of Network Structure on Glass Transition Temperature of Elastomers. *Materials* **2016**, *9*, No. 607.

(86) Basterra-Beroiz, B.; Rommel, R.; Kayser, F.; Valentín, J. L.; Westermann, S.; Heinrich, G. Revisiting Segmental Order: A Simplified Approach for Sulfur-Cured Rubbers Considering Junction Fluctuations and Entanglements. *Macromolecules* **2018**, *51*, 2076−2088.

(87) Galimberti, M.; Infortuna, G.; Guerra, S.; Barbera, V.; Agnelli, S.; Pandini, S. Sp2carbon Allotropes in Elastomer Matrix: From Master Curves for the Mechanical Reinforcement to Lightweight Materials. *eXPRESS Polym. Lett.* **2018**, *12* (3), 265−283.

(88) Laskowska, A.; Marzec, A.; Boiteux, G.; Zaborski, M.; Gain, O.; Serghei, A. Effect of Imidazolium Ionic Liquid Type on the Properties of Nitrile Rubber Composites. *Polym. Int.* **2013**, *62* (11), 1575−1582.

(89) Marzocca, A. J. Estimation by Mechanical Analysis of the Molecular Parameters of SBR Vulcanizates at Different Cure Conditions. *J. Appl. Polym. Sci.* **1995**, *58* (10), 1839−1845.

(90) Marzocca, A. J.; Goyanes, S. An Analysis of the Influence of the Accelerator/Sulfur Ratio in the Cure Reaction and the Uniaxial Stress-Strain Behavior of SBR. *J. Appl. Polym. Sci.* **2004**, *91* (4), 2601−2609.

(91) Salgueiro, W.; Marzocca, A.; Somoza, A.; Consolati, G.; Cerveny, S.; Quasso, F.; Goyanes, S. Dependence of the Network Structure of Cured Styrene Butadiene Rubber on the Sulphur Content. *Polymer* **2004**, *45* (17), 6037−6044.